bioRxiv preprint doi: https://doi.org/10.1101/2021.10.22.465476; this version posted October 24, 2021. The copyright holder for this preprint (which was not certified by peer review) is the author/funder. All rights reserved. No reuse allowed without permission.

Title: The humanized nanobody RBD-1-2G tolerates the spike N501Y mutation to neutralize SARS-CoV-2

Authors: Ying Fu[1†], Juliana da Fonseca Rezende e Mello[2†], Bryan D. Fleming[1†], Alex Renn[1†], Catherine Z. Chen[1], Xin Hu[1], Miao Xu[1], Kirill Gorshkov[1], Quinlin Hanson[1], Wei Zheng[1], Emily M. Lee[1], Lalith Perera[2], Robert Petrovich[2], Manisha Pradhan[1], Richard T. Eastman[1], Zina Itkin[1], Thomas Stanley[2], Allen Hsu[2], Venkata Dandey[2], William Gillette[3], Troy Taylor[3], Nitya Ramakrishnan[3], Shelley Perkins[3], Dominic Esposito[3], Eunkeu Oh[4], Kimihiro Susumu[5], Mason Wolak[4], Marc Ferrer[1], Matthew D. Hall[1]*, Mario J. Borgnia[2]*, and Anton Simeonov[1]*

Affiliations:

[1] National Center for Advancing Translational Sciences, National Institutes of Health, Rockville, Maryland, USA.

[2] Genome Integrity and Structural Biology Laboratory, National Institute of Environmental Health Sciences, National Institutes of Health, Department of Health and Human Services, Research Triangle Park, NC, USA.

[3] Protein Expression Laboratory, NCI RAS Initiative, Cancer Research Technology Program, Frederick National Laboratory for Cancer Research, Frederick, MD, USA.

[4] Optical Sciences Division, Code 5600, Naval Research Laboratory, Washington, D.C., USA.

[5] Jacobs Corporation, Hanover, Maryland, USA.

*Corresponding author Email: hallma@mail.nih.gov, Mario.Borgnia2@nih.gov, asimeono@mail.nih.gov

[†]These authors contributed equally: Ying Fu, Juliana da Fonseca Rezende e Mello, Bryan D Fleming and Alex Renn

Abstract: Neutralizing antibodies targeting the SARS-CoV-2 spike protein have shown a great preventative/therapeutic potential. Here, we report a rapid and efficient strategy for the development and design of SARS-CoV-2 neutralizing humanized nanobody constructs with sub-nanomolar affinities and nanomolar potencies. CryoEM-based structural analysis of the nanobodies in complex with spike revealed two distinct binding modes. The most potent nanobody, RBD-1-2G(NCATS-BL8125), tolerates the N501Y RBD mutation and remains capable of neutralizing the B.1.1.7 (Alpha) variant. Molecular dynamics simulations provide a structural basis for understanding the neutralization process of nanobodies exclusively focused on the spike-ACE2 interface with and without the N501Y mutation on RBD. A primary human airway air-lung interface (ALI) *ex vivo* model showed that RBD-1-2G-Fc antibody treatment was effective at reducing viral burden following WA1 and B.1.1.7 SARS-CoV-2 infections. Therefore, this presented strategy will serve as a tool to mitigate the threat of emerging SARS-CoV-2 variants.

One-Sentence Summary: A cost-effective, high-throughput, adaptable pipeline capable of identifying effective humanized nanobodies against SARS-CoV-2.

bioRxiv preprint doi: https://doi.org/10.1101/2021.10.22.465476; this version posted October 24, 2021. The copyright holder for this preprint (which was not certified by peer review) is the author/funder. All rights reserved. No reuse allowed without permission.

INTRODUCTION

The severe acute respiratory syndrome-coronavirus 2 (SARS-CoV-2) pandemic led to a worldwide emergency imposing massive strains on medical systems and a staggering number of deaths (*1, 2*). The scientific community responded with unprecedented celerity to develop effective vaccines conferring protective immunity (*3*). Although vaccination reduces the occurrence of severe disease and hospitalizations, there is potential for the emergence of escape variants and ongoing viral transmission (*4*). Thus, there remains an ongoing need for cost-effective, high-throughput, adaptable pipelines capable of identifying effective therapeutics against SARS-CoV-2 and other emerging pandemic threats.

SARS-CoV-2 entry into host cells relies upon the envelope-anchored spike (S) glycoprotein. This large trimeric class I protein densely decorates the viral surface, recognizes host angiotensin-converting enzyme 2 (ACE2), and contains the fusion machinery needed for viral entry (*5, 6*). During biogenesis, each S protomer in the mushroom shaped trimer is cleaved by cellular furin into S1 and S2 subunits responsible for target recognition and fusion, respectively. Each N-terminal S1 subunit contains a receptor binding domain (RBD) targeting the ACE2 on the host cell (*7*). The RBD is connected to a hinge that enables its transition between an 'up' state capable of binding to ACE2 and a 'down' state in which the interaction with the receptor is hindered by the proximity of the adjacent RBD. Receptor binding in the 'up' position triggers a cascade of events including the TMPRSS2-mediated cleavage of the stalk forming S2 protomers to reveal hydrophobic fusion peptides (FP) at each N-terminus of a long axial three helix bundle. Insertion of FPs into the membrane of the target cell is followed by a massive structural rearrangement resulting in its apposition with the viral envelope that leads to their fusion (*8*). Mutations in this targeting/fusion machine have been implicated in increased viral infectivity (*9*). As the driver of viral tropism, the RBD of the surface-exposed S protein is the focus of intense interest for the development of neutralizing antibodies and immunogens (*10*). Multiple variants of SARS-CoV-2 have arisen independently in which N501, one of several key contact residues within the RBD, has been mutated to tyrosine (N501Y). This mutation increases binding affinity to human ACE2 (*11*). These variants have multiple mutations in spike, which have been associated with increased transmission rates and reduced antibody neutralization (*11*). Structural insights into how antibodies bind to SARS-Cov-2 variants are still needed (*12*).

Anti-SARS-CoV-2 RBD neutralizing antibodies isolated from different platforms have been reported (*13*). Nanobodies are a unique class of heavy chain-only antibodies present in *Camelidae* and some shark species. Nanobodies (VHHs) and shark variable new antigen receptors (VNARs) are one order of magnitude smaller than their full-length IgG counterparts. The advantages of using nanobodies as anti-viral biologics are convenient bulk production at multi-kilogram scale in prokaryotic systems, long shelf-life, and greater permeability in tissues (*14, 15*). Nanobodies could be administered orally (e.g. V565 for gastrointestinal tract delivery) or through inhalation (e.g. ALX-0171), which are routes of administration that would be relevant for the COVID-19 pandemic (*16, 17*). The limitation of low affinity from synthetic nanobody libraires could be overcome by affinity maturation and/or constructing multi-valent/paratopic modalities (*18*).

Here, we report a rapid and efficient method of identifying neutralizing nanobodies directed against the SARS-CoV-2 from building nanobody phage display libraries, to *in vitro* and *ex vivo* high-throughput screenings. Synthetic humanized nanobody libraries were constructed by combining a framework with randomized complementarity-determining regions (CDRs) to

bioRxiv preprint doi: https://doi.org/10.1101/2021.10.22.465476; this version posted October 24, 2021. The copyright holder for this preprint (which was not certified by peer review) is the author/funder. All rights reserved. No reuse allowed without permission.

diversify antigen recognition. Ten enriched RBD binders, among which the most potent, RBD-1-2G(NCATS-BL8125) and RBD-2-1F, exhibited an IC_{50} of 490 and 470 nM against SARS-CoV-2 pseudotyped particles, respectively. Constructing bi- or tri-valent formats of the RBD-1-2G domain resulted in improved affinity and neutralization potency against pseudotyped particles and authentic SARS-CoV-2 virus. Furthermore, cryo-electron microscopy (cryo-EM) structures for four nanobodies in complex with a stabilized SARS-CoV-2 S-protein ectodomain (*19*) revealed two distinct binding modes. The epitope for 'Group 1' nanobodies overlaps the receptor binding motif (RBM) at the distal end of the RBD. 'Group 2' binders targeted epitopes on the flat area proximal to the N-terminal domain of the adjacent monomer. This binding site was found to not overlap with the RBM and failed to inhibit ACE binding. Additionally, cryo-EM showed that three copies of RBD-1-2G were capable of binding to the same spike trimer. The RBD-1-2G nanobody was capable of neutralizing pseudotyped particles containing the N501Y mutation. A primary human airway air-liquid interface tissue model demonstrated that RBD-1-2G-Fc treatment was able to reduce viral burden in both WA1 and B.1.1.7 infections. Molecular dynamics simulation provides insights for nanobodies binding epitope exclusively focused on the spike-ACE2 interface. RBD-1-2G's residues in the complementarity-determining region 3 (CDR3) contribute substantially to the neutralization of the wild-type (WT) SARS-CoV-2 and the B.1.1.7 alpha variant (N501Y). This approach could greatly apply to mitigate other infectious diseases.

RESULTS

Identification of SARS-CoV-2 neutralizing VHHs from synthetic, humanized nanobody libraries

To develop a platform for rapid nanobody discovery, we first designed a number of synthetic phage-displayed nanobody libraries, starting from a backbone derived from the first approved nanobody drug, caplacizumab (Fig. 1A). The caplacizumab framework region was combined with synthetized complementarity-determining loops (CDRs) to diversify the highly variable antigen-binding interface of the nanobody (*20*). This resulted in libraries each with diversity of $>10^{10}$ transformants. Phage panning was performed for one round against S1 domain of SARS-CoV-2 spike, with two additional panning rounds against RBD of SARS-CoV-2 (Fig. 1B). A total of 13 nanobodies were identified during the panning process, with 10 of these showing sequence enrichment (Supplemental Table 1). Nanobodies were produced in *Vibrio natriegens* and purified using Ni-NTA affinity chromatography followed by size exclusion chromatography (Fig. S1A-B). Nanobody size and MW were confirmed by SDS-PAGE and high-resolution MS (Fig. S1C-D). bio-layer interferometry (BLI) analysis was used to visualize real time association and dissociation of RBD-mFc and S1-hFc to the various nanobodies. Profiles for RBD-1-1E, RBD-2-1F and RBD-1-2G can be found in Figure 1C. Global fit modeling revealed binding affinities of 0.9 nM (RBD-1-1E), 4.9 nM (RBD-2-1F) and 9.4 nM (RBD-1-2G) towards RBD-mFc (Fig. 1D, Fig. S2). When S1-hFc was used as the analyte, RBD-1-2G showed an affinity of 6.9 nM, a 26.6% improvement (6.9 nM vs 9.4 nM) over the RBD-mFc analyte. Reduced binding affinity was observed for both RBD-2-1F (24.6 nM vs 4.9 nM) and RBD-1-1E (3.8 nM to 0.9 nM) when switching to the S1 format (Fig. 1D, Fig. S3). The observed differences on affinity are probably due to the binding epitope on RBD being less accessible in the context of dimerized S1-hFc. To evaluate whether these nanobodies inhibit RBD-ACE2 complex formation, an AlphaLISA was developed (*21*). ACE2-Avi and RBD-Fc association was determined in the presence of increasing concentration of nanobodies to evaluate their receptor-blocking capabilities (Fig. 1E). Despite RBD-1-2G having the second highest affinity for S1-hFc, it yielded a lower IC_{50} than RBD-1-1E (28.3 nM vs. 126

bioRxiv preprint doi: https://doi.org/10.1101/2021.10.22.465476; this version posted October 24, 2021. The copyright holder for this preprint (which was not certified by peer review) is the author/funder. All rights reserved. No reuse allowed without permission.

nM) (Fig. 1E). These results support RBD-1-2G as a potential candidate for therapeutic development.

Multimerization of RBD-1-2G to improve neutralization of SARS-CoV-2 virus.

To further evaluate RBD-1-2G and to increase SARS-CoV-2 neutralization performance, we constructed bivalent and trivalent modalities. The bivalent format, RBD-1-2G-Fc, had an improved binding affinity of 1.9 nM compared to the monovalent format with 14.3 nM (Fig. 2A, Fig. 2B). The trivalent format (RBD-1-2G-Tri) was constructed through the linking of three monovalent formats with $(GGGGS)_3$ flexible linkers. This further improved the apparent affinity to 0.1 nM for RBD binding (Fig. 2C).

To test if this improved affinity would translate to improved therapeutic potential, we first performed an endocytosis assay using SARS-CoV-2 RBD quantum dots (QD_{608}-RBD) (Fig. S4, Fig. S5) (*22*). RBD-1-2G showed the highest potency with an IC_{50} of 390 nM (Fig. 2D). Conversion of RBD-1-2G to the Fc format reduced the IC_{50} to 14 nM (Fig. 2E). A similar trend was observed for RBD-1-1E-Fc (3728 nM to 32 nM), but not for RBD-2-1F-Fc (947 nM to 3883 nM) (Fig. 2D, Fig. 2E). Despite RBD-2-1F having a better affinity than RBD-1-2G as nanobodies (4.9 nM vs 9.4 nM, Fig. 1D), RBD-1-2G-Fc showed higher affinity than RBD-2-1F-Fc (Fig. S6). The binding of RBD-2-1F to RBD may be inhibited by the presence of a Fc domain.

In vitro neutralization assays using SARS-CoV-2 S-protein pseudotyped murine leukemia virus (MLV) vector particles were employed to further characterize the antiviral activity (*23*). RBD-1-2G was found to neutralize SARS-CoV-2 pseudotyped viruses with an IC_{50} of 490 nM (Fig. 2F). Significant improvements were seen with the Fc and trimer modalities showing inhibition at 88 nM (RBD-1-2G-Fc) and 4.1 nM (RBD-1-2G-Tri) (Fig. 2G, Fig. S7). Consistent with the QD internalization assay, RBD-2-1F-Fc showed improvement over RBD-2-1F but failed to neutralize better than the RBD-1-2G modalities (Fig. 2F). The other nanobodies and Fc modalities tested showed much less potency (Fig. S7). A SARS-CoV-2 live virus screen was performed to assess the neutralizing effect of nanobodies. RBD-1-2G-Tri produced an IC_{50} of 182 nM, followed closely by RBD-1-2G-Fc with an IC_{50} of 255 nM (Fig. 2H). The trimer and Fc modalities of RBD-1-2G were found to be more potent than RBD-1-2G (IC_{50}=1211 nM) and the RBD-2-1F-Fc (IC_{50}=3574 nM). These data support RBD-1-2G and its multimeric modalities for further development as SARS-CoV-2 therapeutics.

RBD-1-2G displays low off-target binding

A human membrane proteome array (MPA, approx. 6,000 human membrane proteins + SARS-CoV-2 spike protein) was used to screen and evaluate potential poly-reactivity and non-specificity of RBD-1-2G. The MPA screen confirmed high-specificity binding of RBD-1-2G to SARS-CoV-2 spike with minimal binding to extraneous human membrane proteins (Fig. S8A). Binding to *mitochondrial elongation factor 1* (MIEF1), an intracellularly expressed protein, was detected in an initial screen. Validation of this target revealed that RBD-1-2G bound MIEF1-transfected cells in a similar fashion to vector-transfected cells (Fig. S8B). Additionally, since MIEF1 is a mitochondrial protein, it will be unlikely to interfere with a blood infusion or nebulized administration of RBD-1-2G. These assays suggest a minimal potential off-target effects of RBD-1-2G if selected for further development.

bioRxiv preprint doi: https://doi.org/10.1101/2021.10.22.465476; this version posted October 24, 2021. The copyright holder for this preprint (which was not certified by peer review) is the author/funder. All rights reserved. No reuse allowed without permission.

Additionally, we lyophilized RBD-1-2G nanobody and tested the reconstituted nanobody in a similar live virus study. The lyophilization process had little effect on overall activity in the live virus screen, with IC_{50} measuring 5.9 µM for the lyophilized and 14.8 µM in untreated samples (Fig. S9). The ability of RBD-1-2G to retain activity after lyophilization is a positive feature that can be useful in the manufacturing and formation of nanobody-based therapeutics.

Cryo-EM revealed two distinct modes of binding for neutralizing nanobodies

To uncover the region bound by nanobodies, we used single particle cryo-EM to obtain electron scattering density maps of a soluble form of S-protein ectodomain in complex with 4 nanobodies (Fig. 3). Maps of the complexes with RBD-1-2G, RBD-2-1F, RBD-1-1G and RBD-1-3H featured extra density in the RBD region (Fig. 3A). Two additional nanobodies (RBD-2-3A and RBD-2-1B) were tested, but the observed electron densities were found to be similar to unliganded spike (Data Not Shown). Low affinity was also observed when these nanobodies bound S1-hFc by bio-layer interferometry (Fig. 1D), suggesting their epitopes are not accessible in the context of the trimeric spike.

The accessible epitopes can be classified into two groups. ‘Group 1’ comprises the binding area for RBD-1-2G and RBD-2-1F located at the distal end of the ‘up’ RBD in an area that overlaps with the RBM. Nanobodies RBD-1-1G and RBD-1-3H bind to epitopes in ‘Group 2’, exposed on the external face of the erect RBD in an area not overlapping the RBM (Fig. 3A). The atomic model fitting of the spike (PDBID: 6zp0) suggest that the ‘Group 1’ binders overlap with the ACE2 binding site, while ‘Group 2’ binders do not prevent ACE2 binding (Fig. S10). In the down conformation, epitopes of ‘Group 2’ on the RBD are sterically occluded by the NTD of the neighboring monomer, thus nanobodies of this group were only detected when bound to the RBD in the ‘up’ conformation. In contrast, densities corresponding to RBD-1-2G can be detected in the ‘up’ and ‘partial down’ conformations of the RBD. This unique intermediate between the ‘up’ and ‘down’ states allows for the accommodation of three molecules of RBD-1-2G without steric hindrance (Fig. 3B), likely explaining the high activity for RBD-1-2G. In order to improve resolution of the binding area, independent refinement of “RBD down” spike monomers (shown in maroon in Fig. 3C) was carried out using symmetry expansion and signal subtraction with the spike monomer. The obtained map was used the atomic model fitting.

RBD-1-2G binds to WT and B.1.1.7 variant (Alpha) at various physiological pHs

Recently, different strains of SARS-CoV-2 with N501Y mutation have been identified which have been associated with increased transmissibility and a reduction in neutralizing antibody activity (*11, 24*). We exposed biosensor-immobilized RBD-1-2G-Fc to both wildtype and B.1.1.7 mutant (N501Y) S1-His and evaluated the BLI signal. The maximum binding response to WT or B.1.1.7 S1-His during the association phase was graphed over a range of pH conditions (7.4 – 4.0) (Fig. 4A). Similar binding profiles were observed for WT and B.1.1.7, but a stronger signal was observed with B.1.1.7. Strongest bindings were observed between pH 5.0 and 6.0. Binding was detectable down to a pH of 4.5. A similar pattern was observed when RBD-His was used instead of S1-His, although there appeared to be stronger binding to the WT (Fig. 4B). The strongest binding was observed at pH 6.0 with a gradual reduction as pH was lower to 4.0. These data would suggest that the RBD-1-2G may stay bound to SARS-CoV-2 WT and B.1.1.7 variant (Alpha) after internalization while in the endosome (pH = 6.5 – 4.5).

bioRxiv preprint doi: https://doi.org/10.1101/2021.10.22.465476; this version posted October 24, 2021. The copyright holder for this preprint (which was not certified by peer review) is the author/funder. All rights reserved. No reuse allowed without permission.

To better judge how the RBD-1-2G formats would perform as therapeutic agents, we performed a pseudotyped particle assay to compare their neutralization ability against the wild type and B.1.1.7 spike proteins. RBD-1-2G-Tri was found to inhibit the B.1.1.7 pseudotyped particles better than the wildtype particles (0.3 nM vs 4.5 nM) (Fig. 4C, Fig. 4D). RBD-1-2G-Fc (17.5 nM vs 10.2 nM) and RBD-1-2G (746.5 nM vs 511.6 nM) showed similar IC_{50} against the B.1.1.7 variant (Fig. 4C, Fig. 4D). Additionally, RBD-2-1F-Fc was able to inhibit the WT pseudotyped particles but failed to inhibit the B.1.1.7 (Alpha) mutant version (Fig. 4C, Fig. 4D). To better replicate the complex tissues of the mammalian respiratory tract, we designed a 3D tissue model utilizing reconstructed normal human airway (tracheobronchial) air-liquid interface (ALI) tissues. We infected the human airway ALI tissues with 5,000 plaque forming units (PFU) for an approximate multiplicity of infection (MOI) of 0.005 of either WA1 or B.1.1.7 SARS-CoV-2 virus per well, in the presence or absence of the RBD-1-2G nanobody, Fc and trimer constructs. The monovalent nanobody was used at 10,000 nM, with the multivalent Fc and trimer being administered at 1,000 nM. After 72 hours of infection the total RNA was collected, and viral mRNA levels of SARS-N was determined by qRT-PCR. Comparison of the delta Ct values (dCt) revealed a significant reduction in viral mRNA present in the wells. On average the dCt of the WA1 infected cells was around 4 cycles in the virus only treatment group. This was increased to 20.4 (Nanobody), 22.8 (Fc) and 17.2 (Trimer) cycles following treatment (Figure 4E). A similar trend was observed with the B.1.1.7 infected cells, but the cells were found to have higher burdens of viral mRNA. The averaged dCT for the no treatment group was found to be 2.2 cycles, indicating that these cells had roughly 3.5 times the viral mRNA than the WA1 infected wells, indicating a higher infection in B.1.1.7 SARS-CoV-2 infected airway ALI tissues in comparison to WA1 SARS-CoV-2 infected tissues. Treatment of the B.1.1.7 infected cells increased the dCT to 5.7 (Nanobody), 7.0 (Fc) and 2.9 (Trimer) (Figure 4F). The RBD-1-2G-Fc showed better activity than the trimer in the ALI tissue model, indicating that the Fc format might be the most favorable for clinical transition.

Atomic modeling of interactions between RBD-1-2G and RBM

To elucidate the residues that participate in the binding of RBD-1-2G with the RBD regions of WT and B.1.1.7 (Alpha) variant, molecular docking of the RBD-Nanobody(Nb) complex was employed before fitting it to the spike (Fig. S11). The best binding mode was selected by superimposing the docking results with the cryo-EM maps. Next, triplicates of the RBD-1-2G-WT RBD and RBD-1-2G-B.1.1.7 RBD complexes were subjected to over 1 μs molecular dynamic (MD) simulations in solution.

The root mean square deviations (RMSDs) of the complexes in all simulations were low, confirming that the systems were stable (Fig. S12). The consistent pattern of the curve, showing mainly a single jump, indicating at least two possible distributions in both systems (Fig. S12, SET2 and SET3). The highly similar patterns of interactions contribute to a very similar binding mode of RBD-1-2G to both the WT and B.1.1.7 (Alpha) variant. The MD results showed that RBD-1-2G binds in a similar angle to both the WT and B.1.1.7 (Alpha) variant (Figure 5A and 5B). When comparing the position fluctuations per residue in each complex, similar patterns in root mean square fluctuations (RMSFs) (Fig. S13) emerged in both systems, with larger variations shown in two distinct regions bracketing the RBD residues 355 – 375 and 470 – 490 (Fig. 5A, 5B, S13A, S13B).

bioRxiv preprint doi: https://doi.org/10.1101/2021.10.22.465476; this version posted October 24, 2021. The copyright holder for this preprint (which was not certified by peer review) is the author/funder. All rights reserved. No reuse allowed without permission.

CDR1 and CDR3, as well as a few residues in the constant region (R76, N73, and W111), were mainly responsible for the stabilization of the complex based on the individual energies from the MD simulation (Fig. 5C). A few residues in the N-terminal constant region (E1, V2, Q3) and CDR2 (A52 and S53), interact with the RBD in both WT and mutant forms (Fig. 5C). The MM/GBSA method was used to estimate the binding free energy (ΔG binding) for nanobody–RBD complex systems. One thousand configurations were selected at 20 – 30 ns time intervals throughout the MD simulation trajectories to compute the MM/GBSA total free energy difference. As shown in Fig. 5C, the average calculated binding energies of RBD-1-2G in complex with WT RBD is -36.1 kcal/mol, while the B.1.1.7 RBD is −38.9 kcal/mol. A slight increase in the number of pairs of hydrogen bonds or salt bridges was observed in the complex with the mutant RBD compared with the WT complex (Fig. S14). Thus, RBD-1-2G can form stable complexes with both the WT and B.1.1.7 variant, with the variant being slightly favored. The predicted interaction energy provided by each residue showed that the salt bridge between E484 and R76 had the most significant contribution to the free energy of binding in both simulations (Fig. 5C, S15). F27 shows increased interaction with E484 in the B.1.1.7 variant, while S29 and R76 showed decreased interactions (Fig. 5D, S15). The observation of similar binding modes and the activity of these nanobodies against the WT and B.1.1.7 variant is conferred collectively by the above results. However, the conformation adopted for RBD-1-2G in the WT complex shows the salt bridge between E484 and R76 is further stabilized by the interaction of E484 with S25, S28, S29, and G26 in some instances (Fig. 5D, S13, Table S3). These stabilizing interactions were also observed with the B.1.1.7 variant in addition to N73 that was also found to play a role. Interestingly, the N501 residue found in the WT SARS-CoV-2 strain was found to interact with Y99 in the CDR3 region of RBD-1-2G (Fig. 5E). However, when the spike contains the N501Y mutation, the primary interaction residues switch to W111 and G112 to interact with the new tyrosine residue (Fig. 5F). This flexibility in the CDR3 region is characteristic of nanobody binding. This flexibility and ability to compensate for spike protein mutations makes the RBD-1-2G nanobody and the multivalent constructs good choices for therapeutic development.

DISCUSSIONS

In this study, we report the isolation and characterization of SARS-CoV-2 neutralizing single-domain antibodies from a pool of humanized phage libraries. These nanobodies bind the SARS-CoV-2 spike RBD with single-digit nM to μM affinity, and are capable of neutralizing S-protein pseudotyped and authentic viruses in mammalian cell models of SARS-CoV-2 infection.

RBD-1-2G showed the best overall potency and improved viral neutralization when incorporated into bivalent and trivalent modalities. RBD-1-2G binds an epitope on the top of the RBD that overlapped with binding site for ACE2 (Fig. S10). The potency observed for RBD-1-2G was not only attributed to its high affinity, but also due to the ability of this nanobody to bind the RBD in a wide range of conformations from the “up” to the “down” states (Fig. 3B). Recent cryo-EM studies revealed two prevalent states of S trimer: three RBD domains in “down” conformation which may indicate a conformational immune escape mechanism of action (*6*), or only one RBD in the “up” conformation corresponding to the ACE2-accessible state (*6*, *25*). Some nanobodies (Group 2) could not be imaged in multiple RBD conformations, which would suggest that conformation switching to a protected, three RBD down conformation may sterically restrict binding. The ability of RBD-1-2G to bind in both the “up” and “half down” states allow three nanobodies to bind to a single spike trimer regardless of the RBD conformation state.

bioRxiv preprint doi: https://doi.org/10.1101/2021.10.22.465476; this version posted October 24, 2021. The copyright holder for this preprint (which was not certified by peer review) is the author/funder. All rights reserved. No reuse allowed without permission.

The molecular dynamics results provided a deep understanding of how RBD-1-2G interacts with the RBM. This molecule displayed at least two different binding modes, according to the RMSD analysis, which can be related with the low resolution observed in the Cryo-EM map specifically in the RBD and Nb region (Fig. S12). This Nb showed a very similar binding mode to the WT and B.1.1.7 variant, which was also observed in the Cryo-EM maps (Fig. 3B and S16). One of the reasons for the higher affinity of RBD-1-2G to B.1.1.7 RBD could be related to the presence of the tyrosine in position 501, since it is a longer residue than the asparagine residue found in the WT RBD. The tyrosine also displays higher rotational degree of freedom than the asparagine where the sidechain may be slightly dipolar in nature. Even having a flexible side chain, a dipolar asparagine sidechain may not show the same adaptability of the possible hydrogen bonds donors/acceptors as tyrosine. The mutant might favor the formation not just of the hydrogen bond with the Gln109 (as seen in WT) but also with the neighboring residues Gly112 and Trp111, thus slightly increasing the affinity. Overall, the high activity profile and the possibility of binding in different conformations to the RBD, supports the versatility of RBD-1-2G as a good prototype to design new candidates that are capable to adapt to different SARS CoV-2 variants.

The continued spread of SARS-CoV-2 infections around the world, primarily in dense population settings, has resulted in the emergence of new mutant lineages. For this study we used the B.1.1.7/Alpha (N501Y), which enhanced the RBD binding to ACE2 receptor, to determine the effect of the mutation on our nanobody. This variant (in early June 2020) was the dominant strain in the United States (>70% of all sequenced strains). The N501Y mutation has been found in newer variants including the current most dominant strains (*11*). RBD-1-2G was shown to bind both to the N501Y mutant and the WT RBD and that the hydrogen bond interaction with residue 501 is conserved. Nanobody have been shown to be able to recognize epitopes often inaccessible to conventional antibodies which could offer some advantages to target variants (*26*). It has been more challenging to screen antibodies which can bind to RBM but tolerate a mutation. In this work, we demonstrated the mechanism by which a nanobody targeting RBM could accommodate the N501Y mutant. This could pave the road to target other current and future variants. The ability to rapidly screen artificial humanized nanobody libraries to identify compatible binders helps to counter the immunogenic defenses developed by viral pathogens. The method described in this study could also be expanded to infectious diseases other than COVID-19 and serve as a technical reserve for rapid neutralizing nanobodies discovery during future pandemics.

References and Notes

1. E. Dong, H. Du, L. Gardner, An interactive web-based dashboard to track COVID-19 in real time. *Lancet Infect Dis* **20**, 533-534 (2020).
2. S. F. Sia *et al.*, Pathogenesis and transmission of SARS-CoV-2 in golden hamsters. *Nature* **583**, 834-838 (2020).
3. S. S. Abdool Karim, T. de Oliveira, New SARS-CoV-2 Variants — Clinical, Public Health, and Vaccine Implications. *New England Journal of Medicine*, (2021).
4. D. Han, R. Li, Y. Han, R. Zhang, J. Li, COVID-19: Insight into the asymptomatic SARS-COV-2 infection and transmission. *Int J Biol Sci* **16**, 2803-2811 (2020).
5. W. H. Li *et al.*, Angiotensin-converting enzyme 2 is a functional receptor for the SARS coronavirus. *Nature* **426**, 450-454 (2003).
6. A. C. Walls *et al.*, Structure, Function, and Antigenicity of the SARS-CoV-2 Spike Glycoprotein. *Cell* **181**, 281-292 e286 (2020).

bioRxiv preprint doi: https://doi.org/10.1101/2021.10.22.465476; this version posted October 24, 2021. The copyright holder for this preprint (which was not certified by peer review) is the author/funder. All rights reserved. No reuse allowed without permission.

7. J. Lan *et al.*, Structure of the SARS-CoV-2 spike receptor-binding domain bound to the ACE2 receptor. *Nature* **581**, 215-220 (2020).
8. T. Tang, M. Bidon, J. A. Jaimes, G. R. Whittaker, S. Daniel, Coronavirus membrane fusion mechanism offers a potential target for antiviral development. *Antiviral Res* **178**, 104792 (2020).
9. N. G. Davies *et al.*, Estimated transmissibility and impact of SARS-CoV-2 lineage B.1.1.7 in England. *Science* **372**, eabg3055 (2021).
10. R. Yan *et al.*, Structural basis for the recognition of SARS-CoV-2 by full-length human ACE2. *Science* **367**, 1444-1448 (2020).
11. W. Dejnirattisai *et al.*, Antibody evasion by the P.1 strain of SARS-CoV-2. *Cell*, (2021).
12. P. Wang *et al.*, Antibody resistance of SARS-CoV-2 variants B.1.351 and B.1.1.7. *Nature*, (2021).
13. A. Renn, Y. Fu, X. Hu, M. D. Hall, A. Simeonov, Fruitful Neutralizing Antibody Pipeline Brings Hope To Defeat SARS-Cov-2. *Trends in Pharmacological Sciences* **41**, 815-829 (2020).
14. M. Dumoulin *et al.*, Single-domain antibody fragments with high conformational stability. *Protein Sci* **11**, 500-515 (2002).
15. G. Hussack, T. Hirama, W. Ding, R. Mackenzie, J. Tanha, Engineered single-domain antibodies with high protease resistance and thermal stability. *PLoS One* **6**, e28218 (2011).
16. R. Arezumand, A. Alibakhshi, J. Ranjbari, A. Ramazani, S. Muyldermans, Nanobodies As Novel Agents for Targeting Angiogenesis in Solid Cancers. *Front Immunol* **8**, (2017).
17. S. Nambulli *et al.*, Inhalable Nanobody (PiN-21) prevents and treats SARS-CoV-2 infections in Syrian hamsters at ultra-low doses. **7**, eabh0319 (2021).
18. C. J. Bracken *et al.*, Bi-paratopic and multivalent VH domains block ACE2 binding and neutralize SARS-CoV-2. *Nature Chemical Biology* **17**, 113-121 (2021).
19. D. Wrapp *et al.*, Cryo-EM structure of the 2019-nCoV spike in the prefusion conformation. *Science* **367**, 1260-+ (2020).
20. C. McMahon *et al.*, Yeast surface display platform for rapid discovery of conformationally selective nanobodies. *Nat Struct Mol Biol* **25**, 289-+ (2018).
21. Q. M. Hanson *et al.*, Targeting ACE2-RBD Interaction as a Platform for COVID-19 Therapeutics: Development and Drug-Repurposing Screen of an AlphaLISA Proximity Assay. *Acs Pharmacol Transl* **3**, 1352-1360 (2020).
22. K. Gorshkov *et al.*, Quantum Dot-Conjugated SARS-CoV-2 Spike Pseudo-Virions Enable Tracking of Angiotensin Converting Enzyme 2 Binding and Endocytosis. *Acs Nano* **14**, 12234-12247 (2020).
23. C. Z. Chen *et al.*, Identifying SARS-CoV-2 Entry Inhibitors through Drug Repurposing Screens of SARS-S and MERS-S Pseudotyped Particles. *Acs Pharmacol Transl* **3**, 1165-1175 (2020).
24. P. Wang *et al.*, Antibody resistance of SARS-CoV-2 variants B.1.351 and B.1.1.7. *Nature* **593**, 130-135 (2021).
25. D. Wrapp *et al.*, Structural Basis for Potent Neutralization of Betacoronaviruses by Single-Domain Camelid Antibodies. *Cell* **181**, 1004-+ (2020).
26. J. Xu *et al.*, Nanobodies from camelid mice and llamas neutralize SARS-CoV-2 variants. *Nature*, (2021).
27. R. Huang *et al.*, Biological activity-based modeling identifies antiviral leads against SARS-CoV-2. *Nat Biotechnol*, (2021).
28. D. Esposito *et al.*, Optimizing high-yield production of SARS-CoV-2 soluble spike trimers for serology assays. *Protein Expres Purif* **174**, (2020).
29. T. Taylor, J. P. Denson, D. Esposito, Optimizing Expression and Solubility of Proteins in E. coli Using Modified Media and Induction Parameters. *Methods Mol Biol* **1586**, 65-82 (2017).

bioRxiv preprint doi: https://doi.org/10.1101/2021.10.22.465476; this version posted October 24, 2021. The copyright holder for this preprint (which was not certified by peer review) is the author/funder. All rights reserved. No reuse allowed without permission.

30. W. Gillette *et al.*, Production of Farnesylated and Methylated Proteins in an Engineered Insect Cell System. *Methods Mol Biol* **2009**, 259-277 (2019).
31. C. Z. Chen *et al.*, Drug Repurposing Screen for Compounds Inhibiting the Cytopathic Effect of SARS-CoV-2. *Front Pharmacol* **11**, (2021).
32. D. F. Tucker *et al.*, Isolation of state-dependent monoclonal antibodies against the 12-transmembrane domain glucose transporter 4 using virus-like particles. *P Natl Acad Sci USA* **115**, E4990-E4999 (2018).
33. A. Roy, A. Kucukural, Y. Zhang, I-TASSER: a unified platform for automated protein structure and function prediction. *Nat Protoc* **5**, 725-738 (2010).
34. D. A. Case *et al.* (University of California, San Francisco., 2020).

Acknowledgments: We thank all colleagues of the COVID-19 team from NCATS for their support during the study, including Ganesha Bantukallu and Vinoth Chenniappan for help with lyophilizations Bolormaa Baljinnyam for help with initial BLI and nano-DSF efforts, and Paul Shinn for his advice and guidance. We thank Drs. Andrew C. Kruse (Harvard University) and Aaron M. Ring (Yale University) for support and suggestions for constructing the phage libraries. We thank Vanessa Wall, Kelly Snead, Jennifer Mehalko, Matthew Drew, and Simon Messing of the Frederick National Laboratory for scientific support of protein production efforts. We thank Dr. Gary Whittaker (Cornell University) for providing plasmids for pseudotyping.

Funding:
This research was supported in part by the National Center for Advancing Translational Sciences (NCATS), by the NIH Intramural Targeted Anti-COVID-19 (ITAC) Program (ZIAES103341 to M.J.B.), the National Institute of Environmental Health Sciences (ZICES10326 to M.J.B.), and the Intramural Research Program of the NIH. This project has been funded in part with Federal funds from the National Cancer Institute, National Institutes of Health, under contract number HHSN261200800001E and Naval Research Laboratory provided funding via its internal Nanoscience Institute. Reagent preparation was supported via the NRL COVID-19 base fund.

Author contributions:

Conceptualization: YF, MH, MJB, AS

Methodology: YF, BDF, MH, MJB, AS

Investigation: YF, JFR, BDF, AR, CZC, XH, KG, QH, EML, RP, MX, MP, RE, ZI, TS, AH, VD, WG, TT, NR, SP, DE, EO, KS, MW

Visualization: BDF, YF, JFR, AR, MJB

Writing – original draft: YF, BDF, JFR, AR, MH, MJB, AS

Writing – review & editing: BDF, YF, JFR, AR, MH, MJB, AS

Funding acquisition: MH, MJB, AS, MF

Project administration: MH, MJB, AS

Supervision: YF, BDF, MF, MH, MJB, AS

bioRxiv preprint doi: https://doi.org/10.1101/2021.10.22.465476; this version posted October 24, 2021. The copyright holder for this preprint (which was not certified by peer review) is the author/funder. All rights reserved. No reuse allowed without permission.

Competing interests: Y.F., A.R., B.D.F., M.H., and A.S. are listed as inventors on pending patent applications for the listed nanobodies in this work. The other authors declare that they have no competing interests.

Data and materials availability: All data, code, and materials used in the analysis must be available in some form to any researcher for purposes of reproducing or extending the analysis. Include a note explaining any restrictions on materials, such as materials transfer agreements (MTAs). Note accession numbers to any data relating to the paper and deposited in a public database; include a brief description of the data set or model with the number. If all data are in the paper and supplementary materials, include the sentence "All data are available in the main text or the supplementary materials."

Supplementary Materials

Fig S1. Nanobody purification and quality control

Fig S2. Bio-layer interferometry binding profiles for immobilized nanobodies binding RBD-mFc

Fig S3. Bio-layer interferometry binding profile for immobilized nanobodies binding S1-hFc

Fig S4. QD ACE2-GFP endocytosis assay with nanobody treatment

Fig S5. QD ACE2-GFP endocytosis assay with Fc treatment

Fig S6. Global fit curves of 1-2G-Fc and 2-1F-Fc binding to RBD-mFc

Fig S7. SARS-CoV-2 pseudotyped particles assay for non-blocks and the trimer

Fig S8. Cross-reactivity screen of RBD-1-2G

Fig S9. Effect of lyophilization on RBD-1-2G

Fig S10. Atomic fit models of the RBD/ACE2/Nanobody interactions

Fig S11. CryoEM workflow chart and refinement strategy

Fig S12. Root mean square deviation (RMSD) of the MD triplicates

Fig S13. Root mean square fluctuation (RMSF)

Fig S14. Hydrogen bonds and salt bridge interactions per time for the MD stimulations

Fig S15. Free energy of RBD-1-2G binding

Fig S16. Cryo-EM structure of RBD-1-2G bound to B.1.1.7 S protein.

Table S1. Nanobody complementarity-determining regions (CDRs) sequences and phage enrichment stats.

Table S2. Microscope parameters used to collect Cryo-EM data of the nanobody complexes

Table S3. Hydrogen bond distances.

bioRxiv preprint doi: https://doi.org/10.1101/2021.10.22.465476; this version posted October 24, 2021. The copyright holder for this preprint (which was not certified by peer review) is the author/funder. All rights reserved. No reuse allowed without permission.

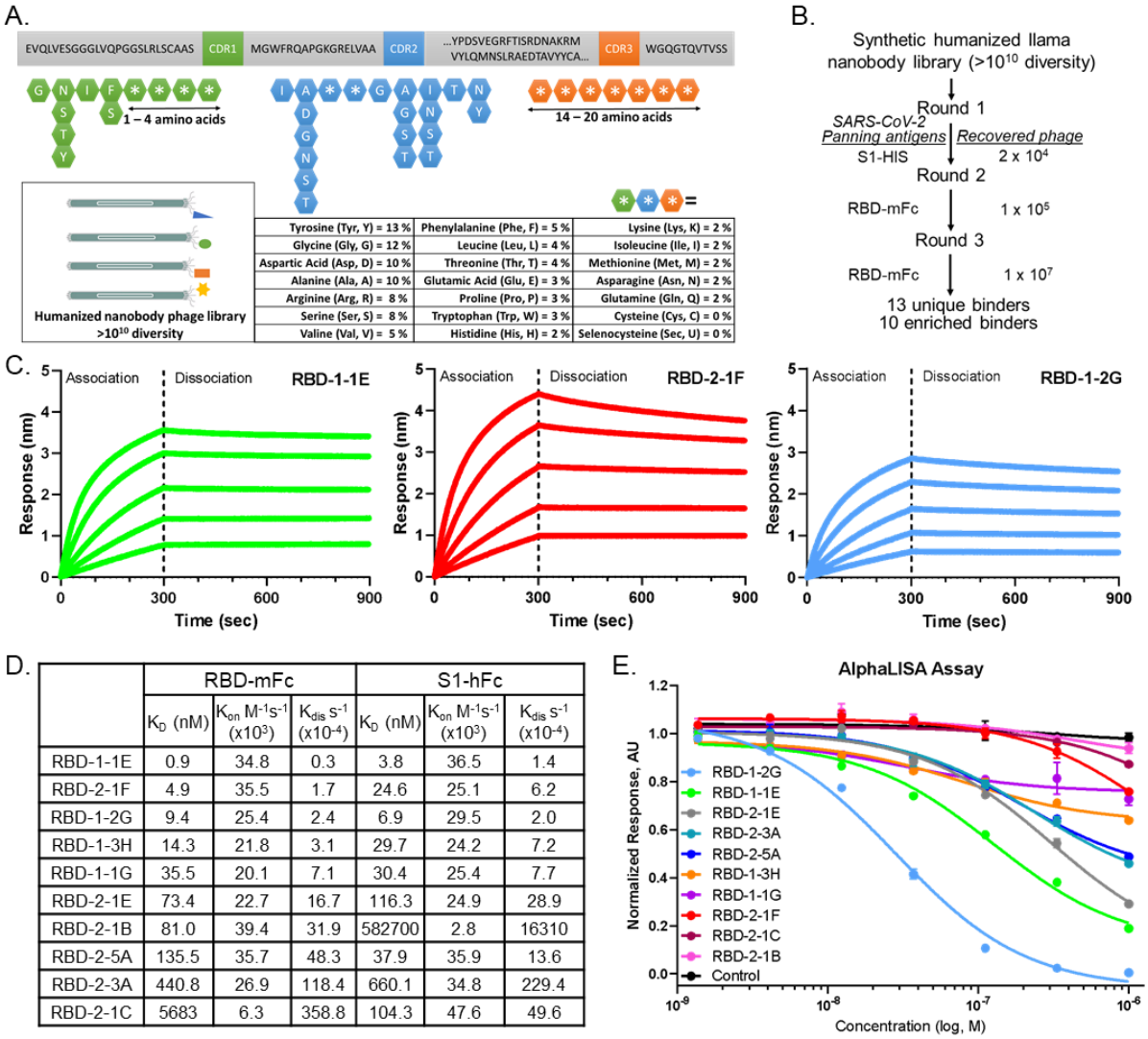

	RBD-mFc			S1-hFc		
	K_D (nM)	K_{on} $M^{-1}s^{-1}$ ($x10^3$)	K_{dis} s^{-1} ($x10^{-4}$)	K_D (nM)	K_{on} $M^{-1}s^{-1}$ ($x10^3$)	K_{dis} s^{-1} ($x10^{-4}$)
RBD-1-1E	0.9	34.8	0.3	3.8	36.5	1.4
RBD-2-1F	4.9	35.5	1.7	24.6	25.1	6.2
RBD-1-2G	9.4	25.4	2.4	6.9	29.5	2.0
RBD-1-3H	14.3	21.8	3.1	29.7	24.2	7.2
RBD-1-1G	35.5	20.1	7.1	30.4	25.4	7.7
RBD-2-1E	73.4	22.7	16.7	116.3	24.9	28.9
RBD-2-1B	81.0	39.4	31.9	582700	2.8	16310
RBD-2-5A	135.5	35.7	48.3	37.9	35.9	13.6
RBD-2-3A	440.8	26.9	118.4	660.1	34.8	229.4
RBD-2-1C	5683	6.3	358.8	104.3	47.6	49.6

Figure 1: Discovery of anti-SARS-CoV-2 Spike RBD nanobodies that block interactions with ACE2. (A) Construction of a synthetic humanized llama nanobody library. (B) Selection strategy for identification of anti-RBD nanobodies using phage panning. (C) Bio-layer interferometry binding profiles of RBD-1-1E, RBD-2-1F and RBD-1-2G against RBD-mFc (200 nM to 12.5 nM, 1:2 dilution). (D) Association (k_{on}) and dissociation (k_{off}) rate constants and equilibrium dissociation constant (K_D) of nanobodies binding to RBD-mFc and S1-hFc. Global fit calculations for RBD-1-1E, RBD-2-1F, and RBD-1-2G used (200 nM to 12.5 nM), with all others using 200 nM to 50 nM. (E) Nanobodies inhibition of RBD-Fc binding to ACE2-Avi using AlphaLISA.

bioRxiv preprint doi: https://doi.org/10.1101/2021.10.22.465476; this version posted October 24, 2021. The copyright holder for this preprint (which was not certified by peer review) is the author/funder. All rights reserved. No reuse allowed without permission.

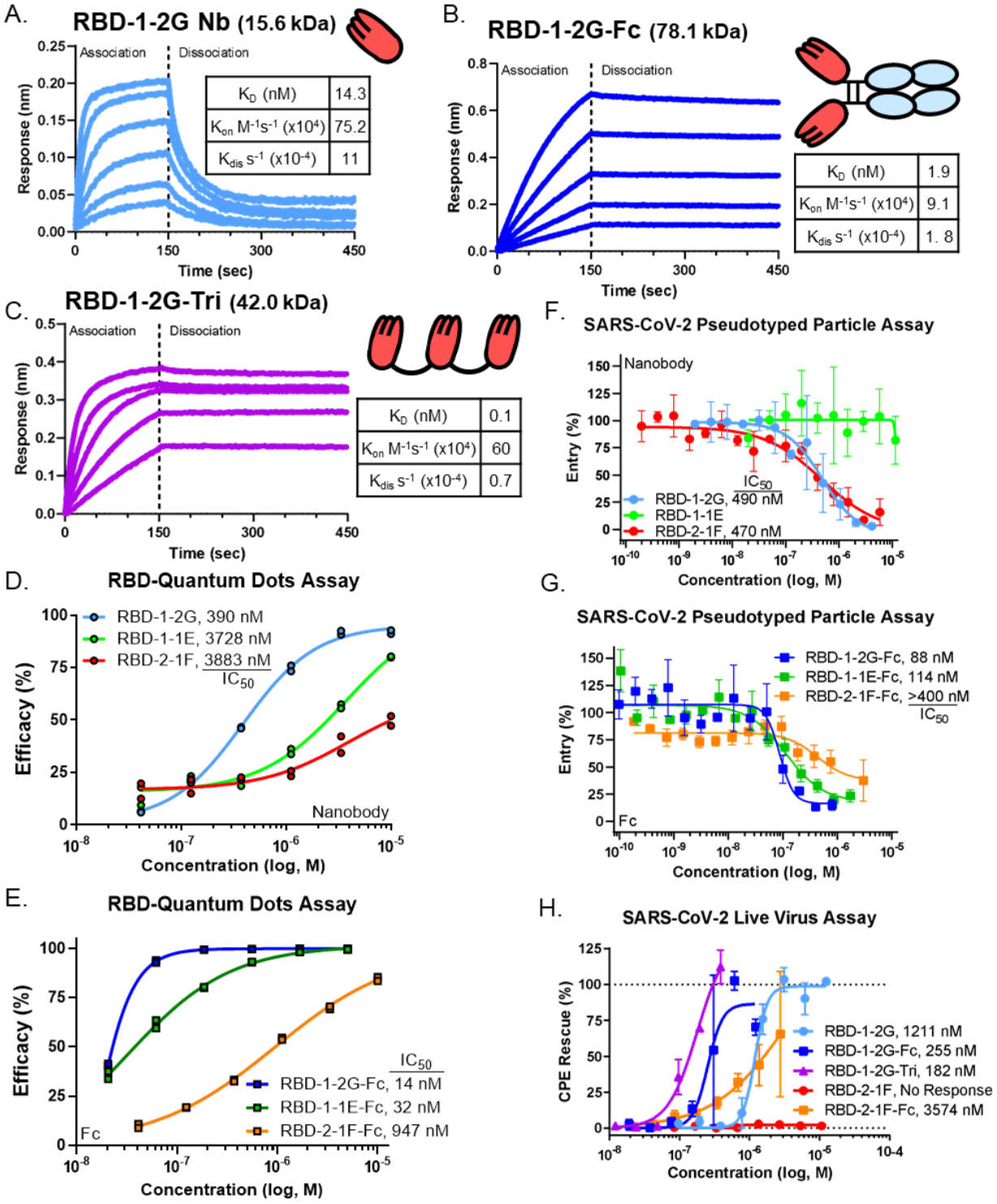

Figure 2: Multivalency improves affinity and inhibition of SARS-CoV-2 infection *in vitro*. (A-C) Bio-layer interferometry binding profiles for the (A) RBD-1-2G Nb, (B) RBD-1-2G-Fc and (C) RBD-1-2G-Trimer against RBD-His (100 nM to 6.25 nM, 1:2 dilution). (D-E) QD endocytosis assay using QD_{608}-RBD and ACE2-GFP HEK293T cells to visualize receptor binding. Nanobody efficacy in reducing RBD internalization by (D) Nanobody and (E) Fc constructs. N = duplicate

bioRxiv preprint doi: https://doi.org/10.1101/2021.10.22.465476; this version posted October 24, 2021. The copyright holder for this preprint (which was not certified by peer review) is the author/funder. All rights reserved. No reuse allowed without permission.

wells, approximately 2500 cells and 1600 cells, respectively. (F-G) SARS-CoV-2 pseudotyped particle entry assay using HEK293-ACE2 cells as target. Inhibition of pseudotyped particle entry was tested for Nanobody(F) and Fc(G) constructs Representative data from two independent experiments. Data represents mean inhibition per concentration (n=3), all error bars represent SEM. Inhibition of SARS-CoV-2 live virus infection with the RBD-1-2G and RBD-2-1F in various formats. Representative biological replicate with n = 2. Technical replicates are n = 2 per concentration, all error bars represent S.D.

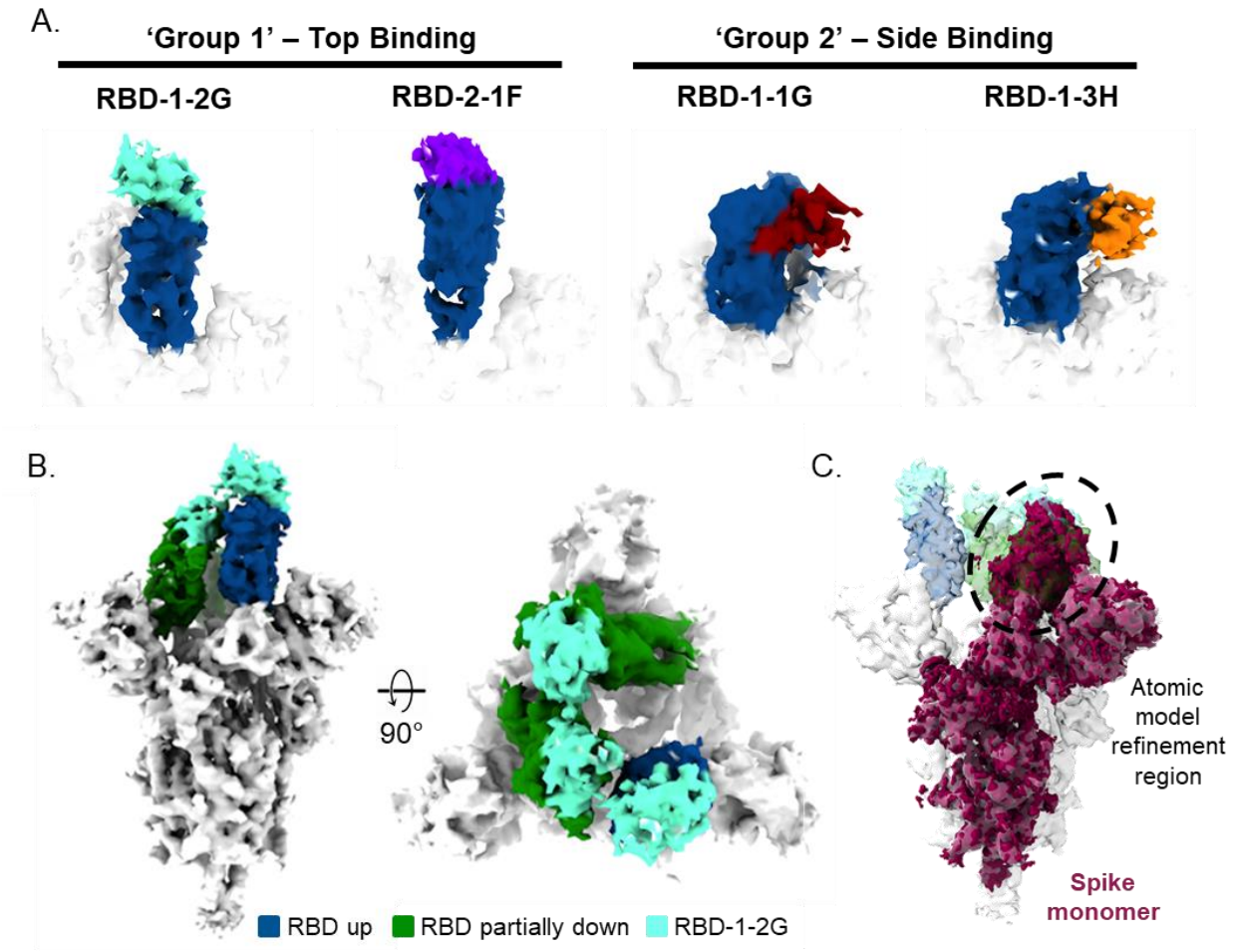

Figure 3: Cryo-EM of SARS-CoV-2 spike trimer and RBD binding nanobodies (A) Cryo-EM analysis of nanobodies complexed with the RBD (up state) revealed two distinct binding modes. (B) Top and side views of the cryo-EM map of S-protein in complex with 3 molecules of RBD-1-2G (cyan). (C) Side view of the S-protein highlighting the spike monomer region refined during image processing is shown. The density containing the RBD in the laid state was used for the atomic model fitting refinement.

bioRxiv preprint doi: https://doi.org/10.1101/2021.10.22.465476; this version posted October 24, 2021. The copyright holder for this preprint (which was not certified by peer review) is the author/funder. All rights reserved. No reuse allowed without permission.

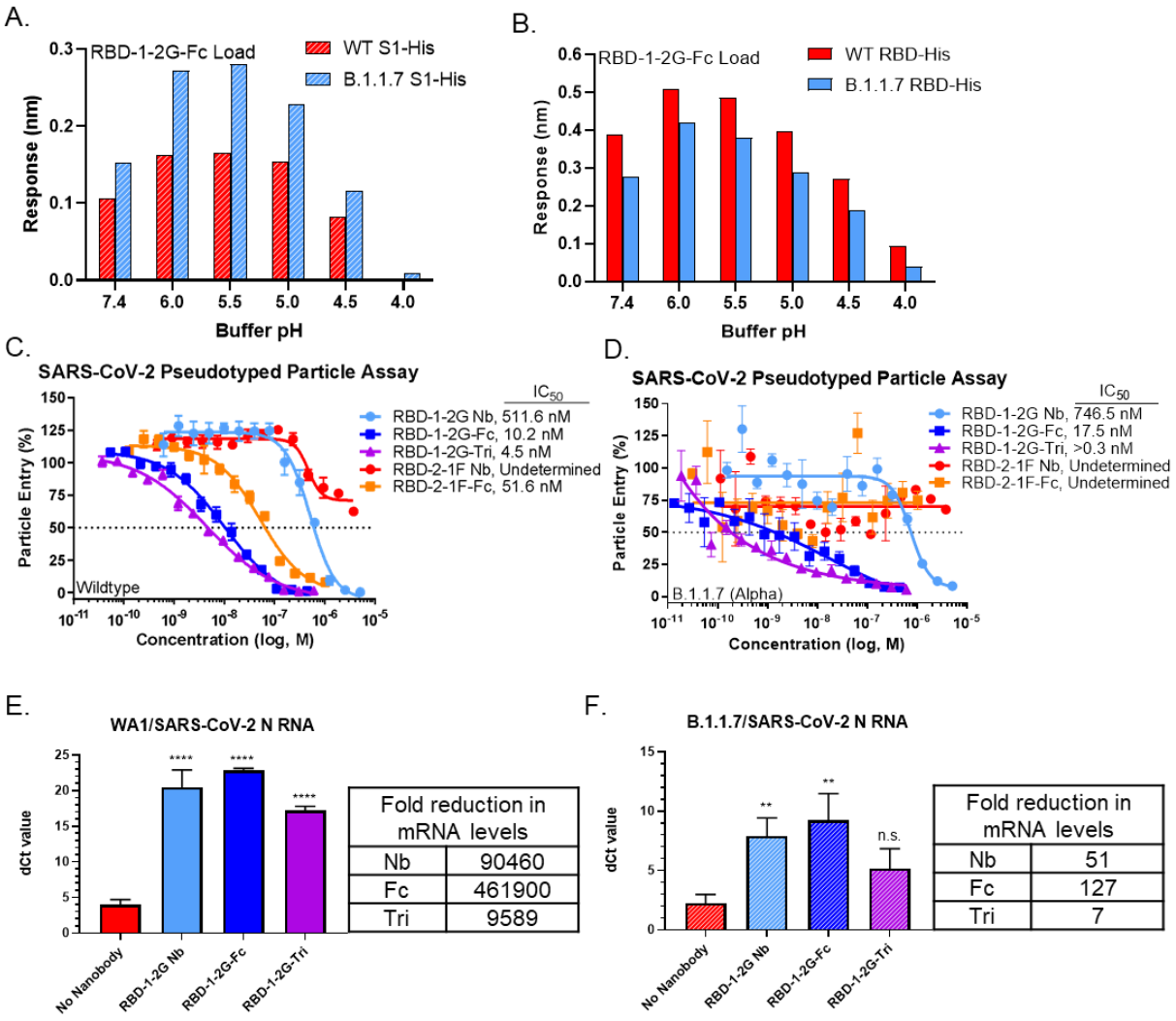

Figure 4: Binding and neutralization of RBD-1-2G to the WT and B.1.1.7 variant (N501Y). (A) Maximum response values reached during the association phase by RBD-1-2G-Fc binding wildtype (WT) and B.1.1.7 (Alpha) variant S1-His. Differences in pH were achieved using PBS (pH 7.4) or 10 mM Acetate buffers with 150 mM NaCl (pH 4 – pH 6.0), all buffers contained 0.1% BSA and 0.02% Tween. (B) Maximum response values reached during the association phase by RBD-1-2G-Fc binding WT and UK variant RBD-His proteins. (C-D) SARS-CoV-2 pseudotyped particle entry assay using HEK293-ACE2 cells as target. Inhibition of WT(C), B.1.1.7 (D) pseudotyped particle treated with various RBD-1-2G and RBD-2-1F formats. Representative biological replicate with n = 2. Technical replicates are n = 3 per concentration, all error bars represent S.D. (E-F) Primary human airway air liquid interface (ALI) model of SARS-CoV-2 infection. Treatment was added at 10,000 nM for nanobody treatment and 1,000 nM for Fc and trimer modalities. Levels of SARS-CoV-2 N mRNA following infection with WA1 (E) or B.1.1.7 (F) SARS-CoV-2 viral infection was determined by qRT-PCR and normalized to 18S mRNA levels. Bars represent that average dCt from biological triplicates, errors bars represent S.D. Fold reduction in mRNA levels are compared to the no nanobody infection control. One-way ANOVA was used to compared treatment groups with the no nanobody control. Significant *p* values are represented as follows: $^{**}p < 0.01$, $^{****}p < 0.0001$, n.s. $p > 0.05$.

bioRxiv preprint doi: https://doi.org/10.1101/2021.10.22.465476; this version posted October 24, 2021. The copyright holder for this preprint (which was not certified by peer review) is the author/funder. All rights reserved. No reuse allowed without permission.

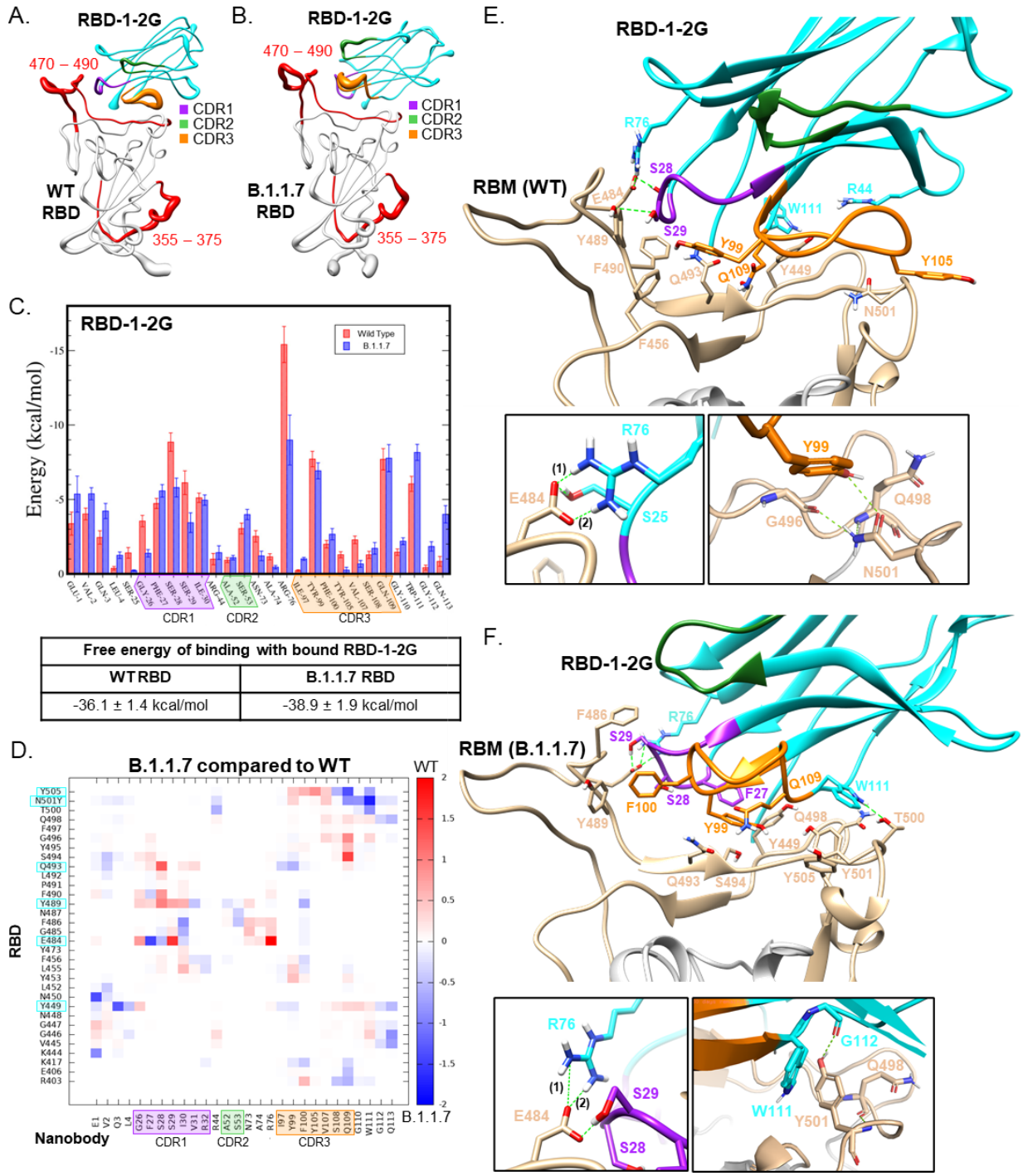

Figure 5: Molecular dynamics of RBD-1-2G with Wild type and B.1.1.7 RBD variant. (A-B) Sausage plot representation of RBD-1-2G in complex with (A)WT RBD and (B) B.1.1.7 RBD. The most flexible regions are indicated in red. (C) Free Energy of binding contribution of each Nb residue in complex with the RBD WT and B.1.17 variant. (D) Heatmap comparing RBD-1-2G's free energy of binding contributions against the B.1.1.7 and WT RBD. RBD residues that contributed greater than -5 kcal/mol are highlighted with cyan. (E-F) Atomic model obtained after

bioRxiv preprint doi: https://doi.org/10.1101/2021.10.22.465476; this version posted October 24, 2021. The copyright holder for this preprint (which was not certified by peer review) is the author/funder. All rights reserved. No reuse allowed without permission.

the atomic model fitting and MD simulations of RBD-1-2G in complex with (E) WT RBD and (F) B.1.1.7 RBD.